Journal of Materials Chemistry A

Unraveling Photoexcitation Dynamics at "Dots-in-a-Perovskite" Heterojunctions from First-Principles

Journal:	*Journal of Materials Chemistry A*
Manuscript ID	TA-ART-05-2019-004871.R1
Article Type:	Paper
Date Submitted by the Author:	17-Jun-2019
Complete List of Authors:	Li, Wei; Hunan Agricultural University, College of Science Zhang, Xu; California State University Northridge, Physics and Astronomy Lu, Gang; California State University Northridge, Physics and Astronomy

Unraveling Photoexcitation Dynamics at "Dots-in-a-Perovskite" Heterojunctions from First-Principles

Wei Li,[1] Xu Zhang,[2] and Gang Lu[2]*

[1]College of Science, Hunan Agricultural University, Changsha 410128, People's Republic of China

[2]Department of Physics and Astronomy, California State University Northridge, Northridge, CA 91330, United States of America

E-mail:

ganglu@csun.edu (G.L.)

Abstract

Both organohalide perovskites and colloidal quantum dots are attractive and promising materials for optoelectronic applications. Recent experiments have combined the two to create "quantum dot-in-perovskite" assemblies for highly efficient light emissions. In this work, we unravel photoexcitation dynamics at the interface between the perovskite and the quantum dot by means of first-principle non-adiabatic molecular dynamics simulations. We find that such assemblies adopt the type-I band structure and are free of defect states. The interfacial and the electronic structure are robust against the thermal fluctuations at 300K. The lowest excitation is predicted to be localized entirely on the quantum dot and the photoexcited charge transfer takes place in a picosecond timescale. The charge transfer dynamics of the photoexcited electron and hole exhibits a moderate asymmetry, which can be attributed to the differences in electronic coupling between the donor and the acceptor and the electron-phonon coupling. The ultrafast and balanced charge transfer dynamics endows the 'dot-in-a-crystal' devices with unprecedented performance, which could lead to important applications in photovoltaics, photocatalysis, and infrared light emissions.

1. Introduction

Hybrid organic-inorganic lead halide perovskites have emerged as one of the most promising materials for optoelectronic applications, including solar cells, light-emitting diodes and lasers, owing to their high optical absorption coefficients, ambipolar charge transport, and long carrier diffusion lengths.[1-3] Colloidal quantum dots (CQDs), on the other hand, are attractive candidates for light-emission applications, thanks to their size-tunable luminescence with high quantum yields and excellent photostability.[4] How to combine the two classes of materials to achieve unprecedented optoelectronic performance thus represents highly appealing but challenging undertaking.

Nonetheless, significant progress has been made recently by Sargent's group who pioneered so-called "dots-in-a-matrix" strategy in which CQDs are embedded in the halide perovskite crystals.[5] The strategy combines the best features of the two – the optical emission properties of the CQDs with the transport properties of the perovskites. Specifically, methylammonium lead triiodide ($MAPbI_3$) was used as the perovskite matrix and PbS as the CQDs. In the epitaxially aligned hetero-crystals, the PbS QDs are fully passivated by the $MAPbI_3$ matrix without the need of conventional organic ligands. The resultant hetero-crystals exhibit remarkable optoelectronic properties: the photo-electrons and holes generated in $MAPbI_3$ can be transferred with 80% efficiency to become excitons in PbS QDs. The photoluminescence quantum efficiency can reach ~9.3%, two orders of magnitude higher than that in the pure QD film.[5] To further improve the interfacial coherence, mixed-halide $MAPbI_xBr_{3-x}$ perovskite was employed to lower the lattice mismatch between PbS QDs.[6] As a result, the external quantum efficiency has increased by more than two-fold.[6] To increase the device stability against heat and moisture, two-

dimensional perovskites were introduced as the matrix for the embedded PbS QDs.[7] The resultant hetero-crystals showed much enhanced stability. More recently, Sargent's group has applied the "dots-in-a-matrix" strategy to thin film solar cells, which led to an impressive power conversion efficiency of 8.95%, a major improvement over previous CQD based photovoltaic devices.[8] Similar perovskite/CQD heterostructures have also been developed for optoelectronic applications, including $CsPbX_3$/ZnS (X=Cl, Br, I) for light emission,[9] $MAPbI_3$/SnS and $CsPbI_3$/PbS for solar cells,[10-11] and $MAPbI_{3-x}Cl_x$/CdSe for electron transport layer.[12] The perovskites have also be combined with *planar* quantum structures, such as graphene and transition-metal dichalcogenides for novel applications.[13-15] Central to the performance of all these heterostructures is interfacial charge transfer dynamics.

The experimental advance has also inspired theoretical investigations on the "dots-in-a-matrix" platform. Insofar, the theoretical effort has been primarily confined to the elucidation of atomic structure and energetics, including band offsets, at the perovskite-QD interfaces.[5, 9, 12, 16] These ground state properties, albeit important, do not probe charge transfer dynamics at the interfaces, which is crucial to the performance of the "dots-in-a-matrix" hetero-crystals. In this paper, we examine the photoexcitation dynamics at the interface between $MAPbI_3$ perovskite and PbS QD via first-principle non-adiabatic molecular dynamics (NAMD) simulations. The timescale for the interfacial charge transfer is established and the phonon modes and electronic states responsible for the charge transfer are identified. The difference in the charge transfer dynamics for the photoexcited electron and hole is rationalized. The theoretical study provides critical insights which are

not readily available from the experiments and guidance for the future development of the "dots-in-a-matrix" devices.

2. Theory and Simulation Methods

A. TDDFT method for exciton charge density

The electronic excitations in semiconductors, such as perovskites and QDs, can be modeled by time-dependent density functional theory (TDDFT). The excited state energies and wavefunctions can be obtained by solving a non-Hermitian eigenvalue equation[17-18]

$$\begin{pmatrix} \tilde{\mathbf{A}} & \tilde{\mathbf{B}} \\ \tilde{\mathbf{B}} & \tilde{\mathbf{A}} \end{pmatrix} \begin{pmatrix} \tilde{\boldsymbol{\psi}}_{\boldsymbol{\alpha}}^{+} \\ \tilde{\boldsymbol{\psi}}_{\boldsymbol{\alpha}}^{-} \end{pmatrix} = \omega_{\alpha} \begin{pmatrix} -\tilde{\mathbf{S}} & 0 \\ 0 & \tilde{\mathbf{S}} \end{pmatrix} \begin{pmatrix} \tilde{\boldsymbol{\psi}}_{\boldsymbol{\alpha}}^{+} \\ \tilde{\boldsymbol{\psi}}_{\boldsymbol{\alpha}}^{-} \end{pmatrix} \tag{1}$$

Here, ω_{α} is αth excitation energy, $\tilde{\boldsymbol{\psi}}_{\boldsymbol{\alpha}}^{\pm}$ is the linear-response orbitals, and $\tilde{S}$ is the overlap operator in the projector augmented wave (PAW) pseudopotentials method.[19] The matrix operators $\tilde{\mathbf{A}}$ and $\tilde{\mathbf{B}}$ act on the linear-response orbitals according to the following equations:

$$\begin{aligned} \left[\tilde{\mathbf{A}}\tilde{\boldsymbol{\psi}}^{\pm}\right]_{i\sigma} &= \sum_j \left(\tilde{H}^{\sigma}\delta_{ij} - \epsilon_{ij\sigma}\tilde{S}\right)|\tilde{\psi}_{j\sigma}^{\pm}\rangle + \sum_{j\tau}\left\langle \tilde{P}_c^{\sigma}\tilde{\psi}_{i\sigma}\middle|\tilde{K}_{\sigma\tau}\middle|\tilde{\psi}_{j\tau}\tilde{P}_c^{\tau}\tilde{\psi}_{j\tau}^{\pm}\right\rangle \\ \left[\tilde{\mathbf{B}}\tilde{\boldsymbol{\psi}}^{\pm}\right]_{i\sigma} &= \sum_{j\tau}\left\langle \tilde{P}_c^{\sigma}\tilde{\psi}_{i\sigma}\middle|\tilde{K}_{\sigma\tau}\middle|\tilde{P}_c^{\tau}\tilde{\psi}_{j\tau}^{\pm}\tilde{\psi}_{j\tau}\right\rangle \end{aligned} \tag{2}$$

where $\tilde{H}^{\sigma}$ is the Kohn-Sham (KS) Hamiltonian. $\epsilon_{ij\sigma}$ and $\tilde{\psi}_{i\sigma}$ are the energy and wavefunction of KS orbitals, respectively. i, and j represent occupied KS orbitals; σ, and τ denote spin. $\tilde{P}_c^{\sigma} = 1 - \sum_i \tilde{S}|\tilde{\psi}_{i\sigma}\rangle\langle\tilde{\psi}_{i\sigma}|$ is the projection operator. $\tilde{K}_{\sigma\tau}$ is the Hartree and exchange-correlation (XC) kernel whose expression can be found elsewhere.[17,20] To calculate the charge density of the αth excited state, we introduce a Lagrangian functional

$$\hat{\mathcal{L}}_{0\alpha}[x,\tilde{\psi},\tilde{\boldsymbol{Z}},\boldsymbol{\Gamma}] = \mathcal{M}_{\alpha\alpha}[x,\tilde{\psi}] + \sum_{ij\sigma}\left\langle \tilde{Z}_{i\sigma}\middle|\left(\tilde{H}^{\sigma}\delta_{ij} - \epsilon_{ij\sigma}\tilde{S}\right)\middle|\tilde{\psi}_{j\sigma}\right\rangle - \sum_{i\geq j,\sigma}\Gamma_{ij\sigma}\left(\langle\tilde{\psi}_{i\sigma}\middle|\tilde{S}\middle|\tilde{\psi}_{j\sigma}\rangle - \delta_{ij}\right) \tag{3}$$

where $\tilde{Z}$ and Γ are Lagrangian multipliers to enforce the Brillouin condition and the orthonormal condition for the KS orbitals, respectively. The detailed description of the Lagrangian functional can be found in our previous publication.[18] The charge density of the excited states can be obtained by the derivative of the Lagrangian functional with respect to the external potential as $\tilde{\rho}_{\alpha}^{\mathrm{ex}} = -\partial\delta\hat{\mathcal{L}}_{0\alpha}/\delta\tilde{V}_{\mathrm{ext}}$.

B. *Ab initio* nonadiabatic molecular dynamics

The charge transfer dynamics is examined by *ab initio* non-adiabatic molecular dynamics (NAMD) combined with the fewest switches surface hoping (FSSH) algorithm in the time-dependent Kohn-Sham framework.[21-23] The time-dependent wavefunction of the excited electron is expanded in terms of its adiabatic Kohn-Sham orbitals at time *t*,

$$\psi_p(\boldsymbol{r},t) = \sum_{k=1}^{N_e} c_{pk}(t)\left|\tilde{\psi}_k(\boldsymbol{r};\boldsymbol{R})\right\rangle \quad (4)$$

Here c_{pk}(t)is time-dependent expansion coefficient, and $\tilde{\psi}_k$(r;R)is the *k*th KS orbital at a given atomic structure $\boldsymbol{R}$. Substitute the Eq. (4) to the time-dependent KS equation:

$$i\hbar\frac{\partial\psi_p(\boldsymbol{r},t)}{\partial t} = \tilde{H}[\rho(\boldsymbol{r},t)]\psi_p(\boldsymbol{r},t) \quad (5)$$

yielding the time evolution of the expansion coefficient:

$$i\hbar\frac{\partial c_{pk}(t)}{\partial t} = \sum_{m=1}^{N_e} c_{pm}(t)\left(\epsilon_m\delta_{km} - i\hbar\boldsymbol{d}_{km}\cdot\dot{\boldsymbol{R}}\right) \quad (6)$$

The last term in the above equation is so-called nonadiabatic coupling (NAC) between the KS orbitals *k* and *m*:

$$\mathrm{NAC} = i\hbar\boldsymbol{d}_{km}\cdot\dot{\boldsymbol{R}} = i\hbar\left\langle\tilde{\psi}_k(\boldsymbol{r};\boldsymbol{R})\middle|\nabla_{\boldsymbol{R}}\middle|\tilde{\psi}_m(\boldsymbol{r};\boldsymbol{R})\right\rangle\cdot\dot{\boldsymbol{R}} = i\hbar\left\langle\tilde{\psi}_k(\boldsymbol{r};\boldsymbol{R})\middle|\frac{\partial}{\partial t}\middle|\tilde{\psi}_m(\boldsymbol{r};\boldsymbol{R})\right\rangle \quad (7)$$

NAC represents the electronic coupling between the KS orbitals in response to nuclear motion. The expansion coefficients and the nonadiabatic coupling are used for the determination of electronic transition rates based on the FSSH method. The classical path

approximation (CPA) is employed here under the assumption that the nuclear dynamics is independent of electronic excitations, but the electronic evolution is affected by the nuclear degree of freedom. Based on CPA, a large number of stochastic realizations in FSSH can be achieved using a single molecular dynamics (MD) trajectory, which greatly reduces the computational cost. This methodology has been widely used to investigate charge transfer processes in a broad range of nanoscale systems.[24-35]

C. Computational details

The planewave PAW pseudopotential DFT method as implemented in Vienna *Ab Initio* Simulation Package (VASP) is used for structural relaxation, electronic structure, and adiabatic molecular dynamics simulations.[36-39] Generalized gradient approximation with Perdew-Burke-Ernzerhof (PBE) functional is used to account for the exchange and correlation contribution to the electronic energy.[40-41] 400 eV cutoff energy is employed. Due to the unique 3D-0D heterostructure, large supercell with more than 700 atoms were adopted in the calculations. As a result, only the Gamma point is sampled in the Brillouin zone to minimize spurious interactions between the supercells. The system is heated to 300 K by a repeated velocity rescaling starting from the optimized structure at 0 K. Subsequently, 1 picosecond (ps) long MD trajectory is generated using the Verlet algorithm with 1 femtosecond (fs) time step. 250 initial conditions sampled from each adiabatic MD trajectory are used to create the ensemble averages for NAMD; 1000 stochastic realizations for the surface hopping processes are employed. For the calculation of the exciton charge density, 24 valance bands are included in the TDDFT calculation, which yield converged energy for the lowest-energy excited state. A uniform background charge is employed to ensure that the net charge of the system remains zero.

3. Results and discussions

To construct a model for the "dots-in-a-matrix" hetero-crystal amenable to first-principles simulations, we first generate a 4×4×4 $MAPbI_3$ supercell as shown in Figure 1a based on the experimental lattice parameter of the cubic $MAPbI_3$ phase.[42] Next, a cavity is created by removing a cube with {100} facets from the perovskite. Finally, a cubic PbS QD with a dimension of ~1.2 nm (Figure 1b) is fully relaxed in vacuum and subsequently inserted into the cavity of the perovskite. The entire computational model has dimensions of 25×25×25 Å and consists of 748 atoms. The perovskite $MAPbI_3$ and PbS QD share the {100} interfaces.

The key feature of the "dots-in-a-matrix" hetero-crystals is the structural affinity between the two constituents. The perovskite $MAPbI_3$ and the PbS QD both have six-coordinated Pb atoms with a similar Pb-Pb bond length, leading to nearly coherent interfaces. To confirm the stability of the heterostructure under thermal disturbance, we carry out first-principles molecular dynamics simulations of the hetero-crystal at 300 K. Figure 1b shows the relaxed molecular structure of the hetero-crystal at zero temperature and Figure 1c displays a representative snapshot of the MD trajectory at 300 K. The Pb-Pb bond length at 0 K in $MAPbI_3$ is about 6.4 Å, which is ~6% larger than that in PbS QD. We find that although the thermal fluctuations at 300 K strongly disturb the interfacial coherence, the overall heterostructure remains stable. In general, the organic cations undergo extensive rotational displacement that is coupled to the thermal distortion of Pb-I inorganic cages, consistent with previous theoretical finding.[43] The displacements of I ions are greater than those of Pb ions in $MAPbI_3$ due to the lighter mass of I. The interatomic

distance between Pb and I across the interface is found to be ~3.5 Å, similar to the Pb-I bond length in pristine $MAPbI_3$. As shown in Figure 1(d), chemical bonds with ionic features are formed at the heterojunction, contributing to the interfacial cohesion and charge transfer. Recent experimental observations of high photovoltaic performance based on $CsPbI_3$/PbS "dots-in-a-matrix" can also be attributed to the structural affinity between the two constituents. The lattice constant of cubic $CsPbI_3$ (6.29 Å) is very close to that of cubic $MAPbI_3$ (6.28 Å).

The density of states (DOS) of the $MAPbI_3$-PbS hetero-crystal is calculated at 0 K based on the relaxed atomic structure. As shown in Figure 2, the total DOS is split into contributions from $MAPbI_3$ and PbS. The partial DOS clearly indicates the formation of the type-I band alignment in the hetero-crystal, with the band gap of PbS falling entirely within the gap of $MAPbI_3$. The vanishing DOS in the band gap suggests the absence of "mid-gap" defect states in the hetero-crystal, which attests the fact that the hetero-interface between the QD and the perovskite is well passivated. The projected DOS shows that Pb, I, and S contribute to the states near the band gap, with the conduction band edge (CBE) mainly consisted of Pb 6p orbitals and the valence band edge (VBE) comprised of I 5p and S 3p orbitals, consistent with the previous findings.[44-47] We find that the thermal fluctuations at 300 K narrow the band gap from 1.37 eV at 0 K to 1.01 eV (averaged from the 1 ps MD trajectory), which is in a good agreement with the experimental value of ~1 eV.[5] The tensile strain imposed on the QD by the interfacial lattice mismatch was believed to increase the band gap of the hetero-crystal.[5] However, the strain is expected to be relieved by the thermal fluctuations, thus the band gap at 300K is lowered. We note that the apparent agreement with the experimental band gap is merely fortuitous thanks to the

well-known error cancellation between the neglect of spin-orbit coupling (SOC) effect and the underestimate of the band gap by the DFT calculations.[48-49] We did not consider the SOC correction explicitly in this work because the Rashba/Dresselhaus band splitting (or SOC effect) was shown to vanishe at the Gamma point.[50] Since our calculations were performed at the Gamma point, the SOC effect is negligible.

Thanks to the formation of the type-I band alignment, the photoexcited charge carriers in $MAPbI_3$ could be injected to PbS QD driven by the band offset. To examine the interfacial charge transfer, we need to identify the initial and final states that are most pertinent to the charge transfer process. To this end, we choose the lowest-energy-unoccupied-state whose spatial distribution is primarily (>80%) confined on $MAPbI_3$ (or donor) to represent the photoexcited electron state *before* the charge transfer. Similarly, we choose the highest-energy-occupied-state with >80% spatial distribution on $MAPbI_3$ to represent the photoexcited hole before the charge transfer. For the final state *after* the charge transfer, we choose the lowest-unoccupied-molecular-orbital (LUMO) and the highest-occupied-molecular-orbital (HOMO) of the hetero-crystal to represent the state of the transferred electron and the hole, respectively. These initial and the final states are shown in Figure 3. We find that the HOMO and LUMO levels are entirely localized on the QD (or the acceptor), thus they are a good representation of the final states. Although we focus on the lowest energy excitation in this work, higher energy excitations are also relevant to the interfacial charge transfer. However, since these "hot" excitations would undergo ultrafast relaxation to the band edges before the charge transfer takes place, we do not consider them explicitly here. As a result, the charge transfer timescales determined in this work represent the lower limits.

We have also calculated the charge density of the lowest energy exciton in the $MAPbI_3$-PbS hetero-crystal at both 0 K and 300 K using TDDFT, as shown in Figure 4. The exciton charge density corresponds to the charge density difference between the excited state and the ground state, with the red and blue color representing the density of the excited electron and hole, respectively. Remarkably, at both temperatures, the photoexcited electron and hole are entirely confined to the PbS QD, suggesting that the lowest excitation of the hetero-crystal occurs exclusively in the QD. Hence, there is a *complete* transfer of photoexcitation from the perovskite to the QD and the QD is the sole source of photoluminescence quenching. This results also justifies the choice of the final state as the one localized entirely on the QD. The electron and hole densities are spatially entangled in the QD, which could lead to ultrafast charge recombination.

The above results are also supported by the MD simulations of the hetero-crystal at 300K. More specifically, we calculate the time evolution in the energy of the donor and acceptor states mentioned above. As shown in Figure 5, there is no energy crossing for any of the four states during the MD simulations, suggesting that the type I band offset is preserved for at least 1 ps at 300K. The robustness of the electronic structure is an important feature of the "dots-in-a-matrix" hetero-crystal, which underpins its remarkable properties. We find that the thermal fluctuation of the acceptor states is stronger than that of the donor states, owing to the smaller atomic mass of S ions compared to I ions in the hetero-crystal. We emphasize that the greater energy oscillation is an indication of strong electron-phonon coupling, which has important implications to non-adiabatic charge transfer processes.

In the "dots-in-a-matrix" hetero-crystal, the photoexcitation in the perovskite leads to the formation of excitons in $MAPbI_3$. Due to the small exciton binding energy,[2, 51] the

bound electron-hole pair could easily dissociate into free charge carriers in $MAPbI_3$. The photo-generated electron and hole are injected into the acceptor states of the QD driven by the band offset. Subsequently, the electron and hole can recombine in the QD via the radiative channels, leading to light emission. Thus, ultrafast charge (both electron and hole) transfer from the perovskite to the QD is a key requirement for efficient light emission. In the following, we examine the interfacial charge transfer dynamics by performing the NAMD simulations at 300 K. The charge transfer across the perovskite-QD interface proceeds by a nonradiative relaxation of the photoexcited electron and hole from the perovskite donor to the QD acceptor. The time-dependent population of the transferred electron and hole onto the acceptor is obtained by the FSSH calculations and the results are summarized in Figure 6. The time-dependent population curves are fitted by exponential functions to extract the relaxation times. We find ultrafast transfer for both electron and hole from the perovskite to the QD. In particular, the estimated electron transfer time is ~0.8 ps, two times faster than the estimated hole transfer time (~1.9 ps). The faster dynamics of the electron is due to the stronger coupling and the smaller energy offset between the donor's and acceptor's CBE states. As shown in Figure 3, the electron wavefunction spreads over to both the donor and acceptor, demonstrating a strong coupling between the CBE states on the donor and the acceptor. In contrast, the hole wavefunction is primarily confined to the donor, implying a weaker coupling between the VBE states on the donor and the acceptor. In addition, as shown in Figure 5, the energy offset between the CBE states (photoexcited electron) on the donor and acceptor is considerably smaller than that between the VBE states on the donor and acceptor (photoexcited hole), and this contrast persists throughout the MD simulation timescale of 1 ps. These two factors

(wavefunction overlap and energy offset) explain the faster charge transfer dynamics of the photoexcited electron. However, despite the moderate asymmetry (a factor of two), the charge transfer dynamics of the electron and the hole can still be considered as balanced. Indeed, the ultrafast and nearly balanced interfacial charge transfer underscores the efficient charge transfer and the high photoluminescence quantum efficiency observed in the experiments.[5]

Finally, we identify the phonon modes that drive the non-adiabatic electronic transitions. To this end, we have calculated the phonon spectrum (also known as spectral density) by discrete Fourier transforms (FT) of the autocorrelation function of the energy difference between the representative pairs of electronic states. The spectrum characterizes the phonon frequencies that are involved in the electronic transitions. The intensity of the FT peak reflects the magnitude of non-adiabatic electron-phonon coupling. Particularly, the red curve shows the FT of the energy gap between the hole states on the donor and the acceptor, while the blue curve represents the FT of the energy gap between the electron states on the donor and the acceptor. The energy gaps for the electron and the hole are shown in Figure 5. We observe that both the electron and hole transfers are facilitated by the phonon modes in the low frequency domain (< 500 cm^{-1}), which consists of the stretching modes of Pb-I bonds and the torsion modes of methylammonium cation. As Pb-I bonds are either in $MAPbI_3$ or across the interface, the charge transfer appears to be driven primarily by the lattice vibrations of the perovskite. The participation of the low-energy acoustic modes in the electronic transitions is not surprising owing to the "softness" of the perovskites, similar to the previous findings.[52-53] As shown in Figure 7, a broad spectrum of the phonon modes are involved in the interfacial electron transfer, with a maximum

amplitude three times higher than that for the interfacial hole transfer. The stronger electron-phonon coupling enables the delocalization of the electronic state over the entire hetero-crystal. On the other hand, there is weaker coupling to the lattice vibrations for the hole, which explains its slower dynamics, especially given the initial localization of the hole wavefunction on the donor (Figure 3). The average NAC for the electron and the hole states is estimated as 5.8 and 3.5 meV, respectively, which is consistent with the above analysis.

4. Conclusion

In summary, we have carried out first-principles simulations to unravel the interfacial charge transfer dynamics in the "dots-in-a-matrix" hetero-crystal. We find that Pb-I bonds are formed across the coherent hetero-interfaces. The type-I band structure with the donor states on $MAPbI_3$ and the acceptor states on PbS is revealed in the absence of mid-gap defect states, consistent with the experimental observations. The lowest-energy excitation is found to be localized entirely on the QD. Both the hetero-interface and its electronic structure remain robust under thermal fluctuations at 300 K. The interfacial charge transfer is predicted to be in a ps timescale, with the transfer of the photoexcited electron twice as fast as that of the hole. The difference in the charge transfer dynamics can be rationalized from the donor and the acceptor electronic coupling strength as well as the electron-phonon coupling strength. The wavefunctions of the photoexcited electron are delocalized onto the entire hetero-crystal while the wavefunctions of the photoexcited hole are largely confined to the donor. While the interfacial transfer for both the electron and the hole is facilitated by the phonons, the electron couples more strongly to the low energy

phonon modes, yielding more efficient charge transfer. We believe that the current study fills the critical knowledge gap that is essential to the operating mechanism of the "dots-in-a-matrix" platform. This work could provide useful insights and guidance to the future development of the "dots-in-a-matrix" devices.

Acknowledgements

We acknowledge the startup funding from Hunan Agricultural University (grant Nos. 540499818006 and 18QN02). The work at California State University Northridge was supported by the US National Science Foundation (DMR-1828019).

References

1. Xing, G.; Mathews, N.; Sun, S.; Lim, S. S.; Lam, Y. M.; Gratzel, M.; Mhaisalkar, S.; Sum, T. C. Long-Range Balanced Electron- and Hole-Transport Lengths in Organic-Inorganic $CH_3NH_3PbI_3$. *Science* **2013,** *342*, 344-347.

2. Stranks, S. D.; Eperon, G. E.; Grancini, G.; Menelaou, C.; Alcocer, M. J. P.; Leijtens, T.; Herz, L. M.; Petrozza, A.; Snaith, H. J. Electron-Hole Diffusion Lengths Exceeding 1 Micrometer in an Organometal Trihalide Perovskite Absorber. *Science* **2013,** *342*, 341-344.

3. Stranks, S. D.; Eperon, G. E.; Grancini, G.; Menelaou, C.; Alcocer, M. J.; Leijtens, T.; Herz, L. M.; Petrozza, A.; Snaith, H. J. Electron-hole diffusion lengths exceeding 1 micrometer in an organometal trihalide perovskite absorber. *Science* **2013,** *342*, 341-344.

4. Ngo, T. T.; Mora-Sero, I. Interaction between Colloidal Quantum Dots and Halide Perovskites: Looking for Constructive Synergies. *J Phys Chem Lett* **2019,** *10*, 1099-1108.

5. Ning, Z.; Gong, X.; Comin, R.; Walters, G.; Fan, F.; Voznyy, O.; Yassitepe, E.; Buin, A.; Hoogland, S.; Sargent, E. H. Quantum-dot-in-perovskite solids. *Nature* **2015,** *523*, 324-8.

6. Gong, X.; Yang, Z.; Walters, G.; Comin, R.; Ning, Z.; Beauregard, E.; Adinolfi, V.; Voznyy, O.; Sargent, E. H. Highly efficient quantum dot near-infrared light-emitting diodes. *Nature Photon* **2016,** *10*, 253-257.

7. Yang, Z.; Voznyy, O.; Walters, G.; Fan, J. Z.; Liu, M.; Kinge, S.; Hoogland, S.; Sargent, E. H. Quantum Dots in Two-Dimensional Perovskite Matrices for Efficient Near-Infrared Light Emission. *ACS Photon* **2017,** *4*, 830-836.

8. Yang, Z.; Janmohamed, A.; Lan, X.; Garcia de Arquer, F. P.; Voznyy, O.; Yassitepe, E.; Kim, G. H.; Ning, Z.; Gong, X.; Comin, R.; Sargent, E. H. Colloidal Quantum Dot Photovoltaics Enhanced by Perovskite Shelling. *Nano Lett* **2015,** *15*, 7539-7543.

9. Chen, W.; Hao, J.; Hu, W.; Zang, Z.; Tang, X.; Fang, L.; Niu, T.; Zhou, M. Enhanced Stability and Tunable Photoluminescence in Perovskite $CsPbX_3$/ZnS Quantum Dot Heterostructure. *Small* **2017,** *13*, 1604085.

10. Han, J.; Yin, X.; Nan, H.; Zhou, Y.; Yao, Z.; Li, J.; Oron, D.; Lin, H. Enhancing the Performance of Perovskite Solar Cells by Hybridizing SnS Quantum Dots with $CH_3NH_3PbI_3$. *Small* **2017,** *13*, 1700953.

11. Zhang, X.; Zhang, J.; Phuyal, D.; Du, J.; Tian, L.; Öberg, V. A.; Johansson, M. B.; Cappel, U. B.; Karis, O.; Liu, J.; Rensmo, H.; Boschloo, G.; Johansson, E. M. J. Inorganic

$CsPbI_3$ Perovskite Coating on PbS Quantum Dot for Highly Efficient and Stable Infrared Light Converting Solar Cells. *Adv Energy Mater* **2018,** *8*, 1702049.

12. Zeng, X.; Zhou, T.; Leng, C.; Zang, Z.; Wang, M.; Hu, W.; Tang, X.; Lu, S.; Fang, L.; Zhou, M. Performance improvement of perovskite solar cells by employing a CdSe quantum dot/PCBM composite as an electron transport layer. *J Mater Chem A* **2017,** *5*, 17499-17505.

13. Xia, F.; Mueller, T.; Lin, Y. M.; Valdes-Garcia, A.; Avouris, P. Ultrafast graphene photodetector. *Nat Nanotechnol* **2009,** *4*, 839-43.

14. Chang, Y. H.; Zhang, W.; Zhu, Y.; Han, Y.; Pu, J.; Chang, J. K.; Hsu, W. T.; Huang, J. K.; Hsu, C. L.; Chiu, M. H.; Takenobu, T.; Li, H.; Wu, C. I.; Chang, W. H.; Wee, A. T.; Li, L. J. Monolayer $MoSe_2$ grown by chemical vapor deposition for fast photodetection. *ACS Nano* **2014,** *8*, 8582-90.

15. Ma, C.; Shi, Y.; Hu, W.; Chiu, M. H.; Liu, Z.; Bera, A.; Li, F.; Wang, H.; Li, L. J.; Wu, T. Heterostructured $WS_2/CH_3NH_3PbI_3$ Photoconductors with Suppressed Dark Current and Enhanced Photodetectivity. *Adv Mater* **2016,** *28*, 3683-9.

16. Jung, Y.-K.; Butler, K. T.; Walsh, A. Halide Perovskite Heteroepitaxy: Bond Formation and Carrier Confinement at the PbS–$CsPbBr_3$ Interface. *J Phys Chem C* **2017,** *121*, 27351-27356.

17. Zhang, X.; Zhang, M.; Lu, G. Charge Stripe Formation in Molecular Ferroelectric Organohalide Perovskites for Efficient Charge Separation. *J Phys Chem C* **2016,** *120*, 23969-23975.

18. Zhang, X.; Lu, G. Subspace formulation of time-dependent density functional theory for large-scale calculations. *J Chem Phys* **2015,** *143*, 064110.

19. Blöchl, P. E. Projector augmented-wave method. *Phys Rev B* **1994,** *50*, 17953-17979.

20. Zhang, X.; Lu, G. First-order nonadiabatic couplings in extended systems by time-dependent density functional theory. *J Chem Phys* **2018,** *149*, 244103.

21. Craig, C. F.; Duncan, W. R.; Prezhdo, O. V. Trajectory Surface Hopping in the Time-Dependent Kohn-Sham Approach for Electron-Nuclear Dynamics. *Phys Rev Lett* **2005,** *95*, 163001.

22. Tully, J. C. Perspective: Nonadiabatic Dynamics Theory. *J Chem Phys* **2012,** *137*, 22A301-22A307.

23. Tully, J. C. Molecular-Dynamics with Electronic-Transitions. *J Chem Phys* **1990,** *93*, 1061-1071.

24. Zhang, S.; Jin, H.; Long, C.; Wang, T.; Peng, R.; Huang, B.; Dai, Y. MoSSe nanotube: a promising photocatalyst with an extremely long carrier lifetime. *J Mater Chem A* **2019,** *7*, 7885-7890.

25. Li, Z.; Zhang, X.; Lu, G. Exciton diffusion in disordered small molecules for organic photovoltaics: insights from first-principles simulations. *Journal of physics. Condensed matter : an Institute of Physics journal* **2014,** *26*, 185006.

26. Li, W.; Sun, Y. Y.; Li, L.; Zhou, Z.; Tang, J.; Prezhdo, O. V. Control of Charge Recombination in Perovskites by Oxidation State of Halide Vacancy. *J Am Chem Soc* **2018,** *140*, 15753-15763.

27. Li, W.; Long, R.; Hou, Z.; Tang, J.; Prezhdo, O. V. Influence of Encapsulated Water on Luminescence Energy, Line Width, and Lifetime of Carbon Nanotubes: Time Domain Ab Initio Analysis. *J Phys Chem Lett* **2018,** *9*, 4006-4013.

28. Jankowska, J.; Prezhdo, O. V. Real-Time Atomistic Dynamics of Energy Flow in an STM Setup: Revealing the Mechanism of Current-Induced Molecular Emission. *J Phys Chem Lett* **2018,** *9*, 3591-3597.

29. He, J.; Vasenko, A. S.; Long, R.; Prezhdo, O. V. Halide Composition Controls Electron–Hole Recombination in Cesium–Lead Halide Perovskite Quantum Dots: A Time Domain Ab Initio Study. *J Phys Chem Lett* **2018,** *9*, 1872-1879.

30. He, J.; Fang, W.-H.; Long, R. Unravelling the Effects of A-Site Cations on Nonradiative Electron–Hole Recombination in Lead Bromide Perovskites: Time-Domain ab Initio Analysis. *J Phys Chem Lett* **2018,** 4834-4840.

31. Wei, L.-y.; Ma, W.; Lian, C.; Meng, S. Benign Interfacial Iodine Vacancies in Perovskite Solar Cells. *J Phys Chem C* **2017,** *121*, 5905-5913.

32. Long, R.; Casanova, D.; Fang, W.-H.; Prezhdo, O. V. Donor–Acceptor Interaction Determines the Mechanism of Photoinduced Electron Injection from Graphene Quantum Dots into TiO_2: π-Stacking Supersedes Covalent Bonding. *J Am Chem Soc* **2017,** *139*, 2619-2629.

33. Li, Z.; Zhang, X.; Lu, G. Dipole-Assisted Charge Separation in Organic–Inorganic Hybrid Photovoltaic Heterojunctions: Insight from First-Principles Simulations. *J Phys Chem C* **2012,** *116*, 9845-9851.

34. Nijamudheen, A.; Akimov, A. V. Criticality of Symmetry in Rational Design of Chalcogenide Perovskites. *J Phys Chem Lett* **2017,** 248-257.

35. Senanayake, R. D.; Akimov, A. V.; Aikens, C. M. Theoretical Investigation of Electron and Nuclear Dynamics in the $[Au_{25}(SH)_{18}]^{-1}$ Thiolate-Protected Gold Nanocluster. *J Phys Chem C* **2016**.

36. Kresse, G.; Furthmüller, J. Efficient iterative schemes forab initiototal-energy calculations using a plane-wave basis set. *Phys Rev B* **1996,** *54*, 11169-11186.

37. Kresse, G.; Furthmuller, J. Efficiency of ab-initio total energy calculations for metals and semiconductors using a plane-wave basis set. *Comp Mater Sci* **1996,** *6*, 15-50.

38. Kresse, G.; Hafner, J. Ab initiomolecular-dynamics simulation of the liquid-metal–amorphous-semiconductor transition in germanium. *Phys Rev B* **1994,** *49*, 14251-14269.

39. Kresse, G.; Hafner, J. Ab initiomolecular dynamics for liquid metals. *Phys Rev B* **1993,** *47*, 558-561.

40. Perdew, J. P.; Burke, K.; Ernzerhof, M. Erratum: Generalized gradient approximation made simple. *Phys Rev Lett* **1997,** *78*, 1396.

41. Perdew, J. P.; Burke, K.; Ernzerhof, M. Generalized Gradient Approximation Made Simple. *Phys Rev Lett* **1996,** *77*, 3865-3868.

42. Baikie, T.; Fang, Y. N.; Kadro, J. M.; Schreyer, M.; Wei, F. X.; Mhaisalkar, S. G.; Graetzel, M.; White, T. J. Synthesis and crystal chemistry of the hybrid perovskite (CH3NH3) PbI3 for solid-state sensitised solar cell applications. *J Mater Chem A* **2013,** *1*, 5628-5641.

43. Li, W.; Liu, J.; Bai, F.-Q.; Zhang, H.-X.; Prezhdo, O. V. Hole Trapping by Iodine Interstitial Defects Decreases Free Carrier Losses in Perovskite Solar Cells: A Time-Domain Ab Initio Study. *ACS Energy Lett* **2017,** *2*, 1270-1278.

44. Kim, D.; Kim, D. H.; Lee, J. H.; Grossman, J. C. Impact of stoichiometry on the electronic structure of PbS quantum dots. *Phys Rev Lett* **2013,** *110*, 196802.

45. Yin, W. J.; Shi, T. T.; Yan, Y. F. Unusual Defect Physics in $CH_3NH_3PbI_3$ Perovskite Solar Cell Absorber. *Appl Phys Lett* **2014,** *104*, 063903-063907.

46. He, Y.; Galli, G. Perovskites for Solar Thermoelectric Applications: A First Principle Study of $CH_3NH_3AI_3$(A = Pb and Sn). *Chem Mater* **2014,** *26*, 5394-5400.

47. Du, M. H. Efficient Carrier Transport in Halide Perovskites: Theoretical Perspectives. *J Mater Chem A* **2014,** *2*, 9091-9098.

48. Li, W.; Zhou, L.; Prezhdo, O. V.; Akimov, A. V. Spin–Orbit Interactions Greatly Accelerate Nonradiative Dynamics in Lead Halide Perovskites. *ACS Energy Lett* **2018,** *3*, 2159-2166.

49. Even, J.; Pedesseau, L.; Jancu, J.-M.; Katan, C. Importance of Spin–Orbit Coupling in Hybrid Organic/Inorganic Perovskites for Photovoltaic Applications. *J Phys Chem Lett* **2013,** *4*, 2999-3005.

50. Mosconi, E.; Etienne, T.; De Angelis, F. Rashba Band Splitting in Organohalide Lead Perovskites: Bulk and Surface Effects. *J Phys Chem Lett* **2017,** *8*, 2247-2252.

51. Snaith, H. J. Perovskites: The Emergence of a New Era for Low-Cost, High-Efficiency Solar Cells. *J Phys Chem Lett* **2013,** *4*, 3623-3630.

52. Trivedi, D. J.; Wang, L.; Prezhdo, O. V. Auger-mediated electron relaxation is robust to deep hole traps: time-domain ab initio study of CdSe quantum dots. *Nano Lett* **2015,** *15*, 2086-2091.

53. Liu, J.; Neukirch, A. J.; Prezhdo, O. V. Phonon-induced pure-dephasing of luminescence, multiple exciton generation, and fission in silicon clusters. *J Chem Phys* **2013,** *139*, 164303.

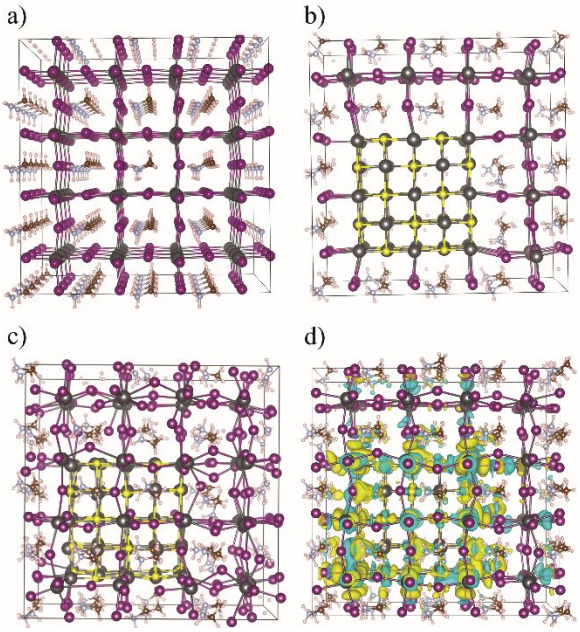

Figure 1. (**a**) The constructed 4×4×4 cubic supercell for $MAPbI_3$ matrix. (**b**) The fully relaxed atomic structure of the $MAPbI_3$-PbS hetero-crystal at 0 K with the interfacial structure clearly presented. (**c**) A representative atomic structure of the hetero-crystal at 300 K obtained from the MD simulations. (**d**) The contour plot showing the bonding charge density for the $MAPbI_3$-PbS hetero-crystal. The charge accumulation and depletion are represented by the blue and yellow color, respectively. The contour isosurface level is set at 0.073 e/bohr^3. The purple, dark gray, yellow, light pink, light blue, dark brown sphere represents I, Pb, S, H, C, N atom, respectively.

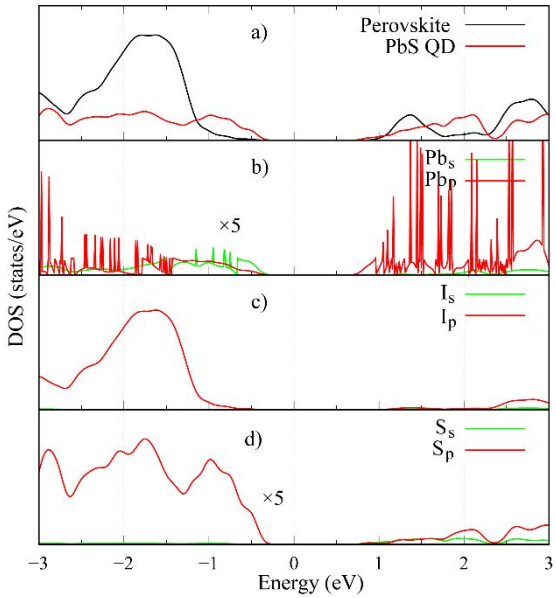

Figure 2. (**a**) The partial density of states (DOS) of the $MAPbI_3$-PbS hetero-crystal projected onto the perovskite (black) and the QD (red). The projected DOS of the hetero-crystal projected onto the Pb (**b**), I (**c**) and S (**d**) atoms.

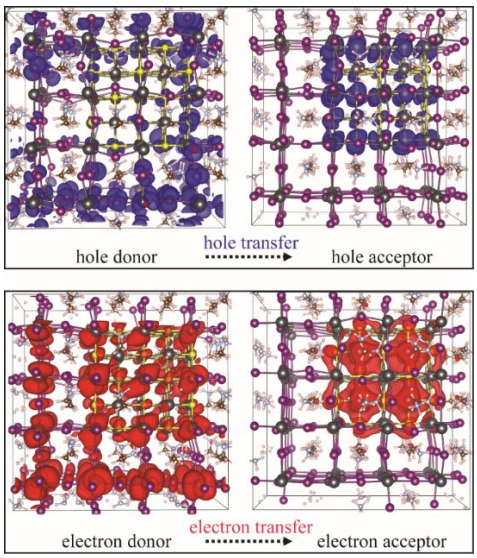

Figure 3. (top panel) The charge density for the photoexcited hole before (left) and after (right) the interfacial charge transfer. (bottom panel) The charge density for the photoexcited electron before (left) and after (right) the interfacial charge transfer.

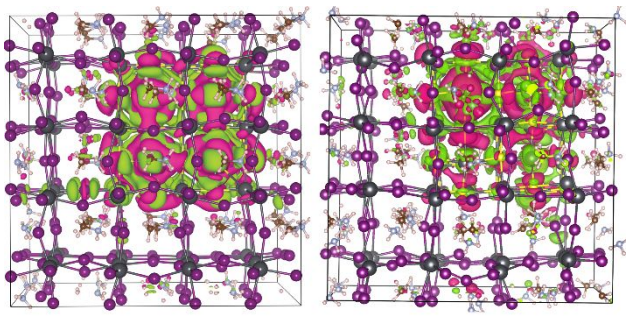

Figure 4. The charge density of the lowest energy exciton for the $MAPbI_3$-PbS hetero-crystal at 0 K and 300 K. The red and blue color represents the electron and hole, respectively.

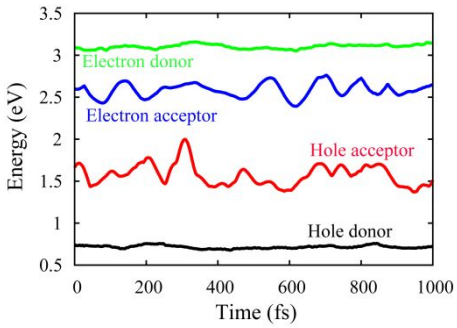

Figure 5. Energy as a function of time for the photoexcited electron and hole states on the donor and the acceptor.

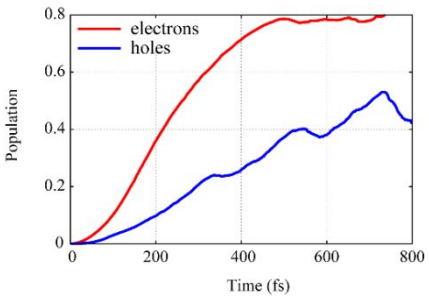

Figure 6. Time evolution for the population (occupation number) of the transferred electron and hole from $MAPbI_3$ to PbS.

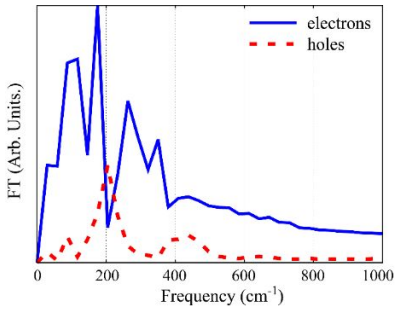

Figure 7. Fourier transform for the time evolution of the electron and the hole energy offset between the donor and the acceptor. The involvement of a broader range of low-frequency vibrations provides additional channels for the electron transfer (blue curve).

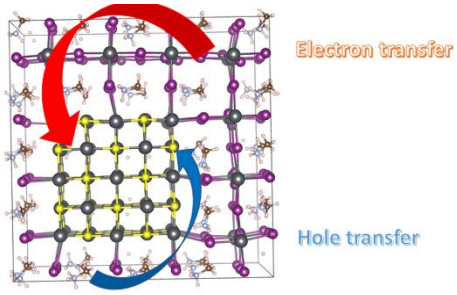

Ultrafast interface charge transfer is observed in “Dots-in-a-Perovskite” Heterojunctions